RSC Advances

PAPER

View Article Online
View Journal | View Issue

Cite this: *RSC Adv.*, 2025, **15**, 38916

Isolation and comprehensive characterization of a bioactive compound from *Garcinia nervosa*: single-crystal X-ray diffraction, antioxidant, protein-binding, and chemosensing studies

Uzma, [a] Mehtab Parveen, *[a] Sabiha Fatima,[b] Avadhesh Kumar, [a] Mohammad Azeem,[a] Masooma Siddiqui [a] and Mahboob Alam *[c]

The study investigates the phytochemical composition and bioactive properties of *Garcinia nervosa*, with a focus on the structural elucidation of isolated compounds and their potential therapeutic applications. Three bioactive compounds, *Gn*-01, *Gn*-02, and *Gn*-03, were isolated from the leaves of *G. nervosa*. *Gn*-01, a known isoflavone named as bergenin, is reported for the first time from this plant, while *Gn*-03 is newly identified from this plant. These compounds were characterized using UV-Vis, FTIR, NMR, and MS. Single-crystal X-ray diffraction revealed compound *Gn*-01's orthorhombic space group $P2_12_12_1$, with Hirshfeld surface analysis showing significant O···H/H···O interactions that stabilize the crystal structure. *Gn*-01 demonstrated potent antioxidant activity with an IC_{50} of 23.438 μg mL^{-1}, comparable to ascorbic acid, and strong non-intercalative binding to human serum albumin (HSA) with a Stern–Volmer constant (K_{sv}) of 168.3 × 10^4 M^{-1} and a binding constant (K_b) of 3.16 × 10^4 M^{-1}, corroborated by molecular docking studies (binding affinity −7.364 kcal mol^{-1}). Notably, *Gn*-01 acted as a selective and sensitive Cu^{2+} chemosensor *via* a fluorescence turn-on (CHEF) mechanism, forming a 1 : 1 complex (K_b = 1.74 × 10^4 M^{-1}; LOD ≈ 0.221 μM). The combination of first-time crystal structure determination, Hirshfeld surface analysis, antioxidant and HSA-binding activity, and Cu^{2+} chemosensing establishes *Gn*-01 as a novel bifunctional therapeutic agent with complementary antioxidant, protein-binding, and metal-sensing activities. Overall, these findings highlight *Garcinia nervosa* as a valuable source of the multifunctional bioactive molecule bergenin, supporting its chemotaxonomic and pharmacological significance and justifying further pharmacological exploration.

Received 10th July 2025
Accepted 5th October 2025

DOI: 10.1039/d5ra04922a

rsc.li/rsc-advances

1. Introduction

The Clusiaceae (Guttiferae) family includes the genus *Garcinia*, which has about 300 species spread throughout Asia, Africa, South America, and Polynesia.[1] Usually small to medium-sized evergreen trees or shrubs, these species do well in tropical and subtropical regions, with some growing up to 30 meters in height. Many *Garcinia* species bear edible fruits, and *Garcinia mangostana* (mangosteen) is especially notable for its unique flavor and health benefits[2] For centuries, various *Garcinia* species have been utilized in traditional medicine to treat ailments such as diarrhea, skin irritations, earaches, wounds, ulcers, and fevers.[3] Recent research has unveiled the remarkable pharmacological potential of these plants, revealing a wide range of bioactive compounds comprising xanthones, benzophenones, triterpenoids, and biflavonoids, recognized for their anticancer, anti-inflammatory, antibacterial, antiviral, antifungal, anti-HIV, antidepressant, and antioxidant activities.[4,5] Among the various *Garcinia* species, *Garcinia nervosa* has attracted significant interest due to its distinct phytochemical profile. Investigations of its methanolic extracts have identified several bioactive compounds, such as the xanthone narvosaxanthone, biflavonoids, and isoflavones like nervosin, irigenin, and 7-methyltectorigenin, along with chalcones.[6] These compounds have shown promising anticancer and anti-inflammatory activities. Extracts derived specifically from *G. nervosa* have shown potent inhibitory effects on platelet-activating factor (PAF) receptor bindings. Despite these encouraging findings, the medicinal potential of *G. nervosa* remains largely unexplored, underscoring the need for further research to fully assess its therapeutic applications.

Human serum albumin (HSA), the most prevalent protein in human plasma, is essential for the transport of many different compounds, such as hormones, pharmaceuticals, and fatty

[a]*Department of Chemistry, Aligarh Muslim University, Aligarh-202002, India*
[b]*Department of Clinical Laboratory Science, College of Applied Medical Sciences, King Saud University, Riyadh 12371, Saudi Arabia*
[c]*Department of Safety Engineering, Dongguk University WISE Campus, 123 Dongdae-ro, Gyeongju 780714, Gyeongsangbuk-do, Republic of Korea. E-mail: mehtab.organic2009@gmail.com; mahboobchem@gmail.com*

acids.[7,8] Its high binding affinity and widespread distribution make it a critical component in drug delivery and bioavailability.[9–11] The interaction of bioactive molecules with HSA is crucial for determining their pharmacokinetics and therapeutic efficacy.[12,13] By binding to HSA, bioactive compounds benefit from enhanced solubility, prolonged circulation time, and improved tissue distribution. This interaction stabilizes the molecules, regulating their release and availability at target sites, and influences their bioactivity. Research has shown that flavonoids, alkaloids, and xanthones, when bound to HSA, can modulate anticancer, anti-inflammatory, and antioxidant activities, positioning these compounds as promising candidates for drug development.[14–16]

The chemosensing properties of bioactive molecules, particularly their ability to detect and bind to copper ions (Cu^{2+}), have also been the subject of increasing interest[17] Copper is vital for many biological processes, but its imbalance is linked to several diseases, including neurodegenerative disorders such as Alzheimer's and Parkinson's[18,19] As a result, the development of molecular sensors capable of selectively binding Cu^{2+} has become an essential focus of diagnostic and therapeutic research. Bioactive molecules like flavonoids, xanthones, and isoflavones exhibit a strong affinity for Cu^{2+}, functional groups such as hydroxyls, carbonyls, and amines, which form stable coordination complexes with metal ions. These interactions are typically detected using UV-vis spectroscopy and fluorescence assays, which provide insights into Cu^{2+} concentrations in biological systems. The ability of these molecules to bind Cu^{2+} ions holds great promise for applications in regulating metal ion homeostasis, developing sensors, and creating therapeutic strategies for diseases linked to copper dysregulation.[20]

Recent studies have advanced our understanding of the therapeutic potential of *G. nervosa*, leading to the isolation of a promising bioactive compound *Gn*-01, a known isoflavone identified as (3,4,8,10-tetrahydroxy-2-(hydroxymethyl)-9-methoxy-3,4,4*a*,10*b*-tetrahydropyrano[3,2-*c*]isochromen-6(2*H*)-one), which has been previously reported in other plants but was isolated for the first time from *Garcinia nervosa*. It has attracted significant attention due to its remarkable bioactivity.[21–30] In addition to *Gn*-01, the previously reported compound *Gn*-02 ((*E*)-1-(2-hydroxy-4-methoxyphenyl)-3-(4-methoxyphenyl)prop-2-en-1-one) was re-isolated from *Garcinia nervosa*.[31] Moreover, another known compound, *Gn*-03 ((*E*)-1-(2-hydroxy-4,6-dimethoxyphenyl)-3-(4-methoxyphenyl)prop-2-en-1-one) was also isolated for the first time from this plant (Fig. 1), although it has been previously reported from other natural sources and *via* synthetic routes.[32–34] The structural elucidation of *Gn*-01 was achieved using a combination of advanced techniques, including elemental analysis, infrared spectroscopy (IR), ultraviolet-visible spectroscopy (UV), nuclear magnetic resonance (NMR), mass spectrometry (MS), X-ray crystallography, and computational studies.[28,29] These methods provided comprehensive insights into the molecular structure of the compound.[24,25]

Furthermore, protein-binding assays revealed that these compounds interact strongly with human serum albumin (HSA), suggesting their potential to modulate protein functions and influence physiological processes. Molecular docking studies further reinforced these findings by demonstrating favorable binding affinities[35–37] between *Gn*-01 and key biological targets.[26,38] Additionally, antioxidant activity tests highlighted the significant free radical scavenging properties of *Gn*-01, pointing to its possible therapeutic applications in mitigating oxidative stress-related diseases.[30]

Notably, the compound *Gn*-01 also exhibited significant metal-sensing properties, particularly towards Cu^{2+} ions. This metal-ion binding ability of *Gn*-01 suggests its potential for

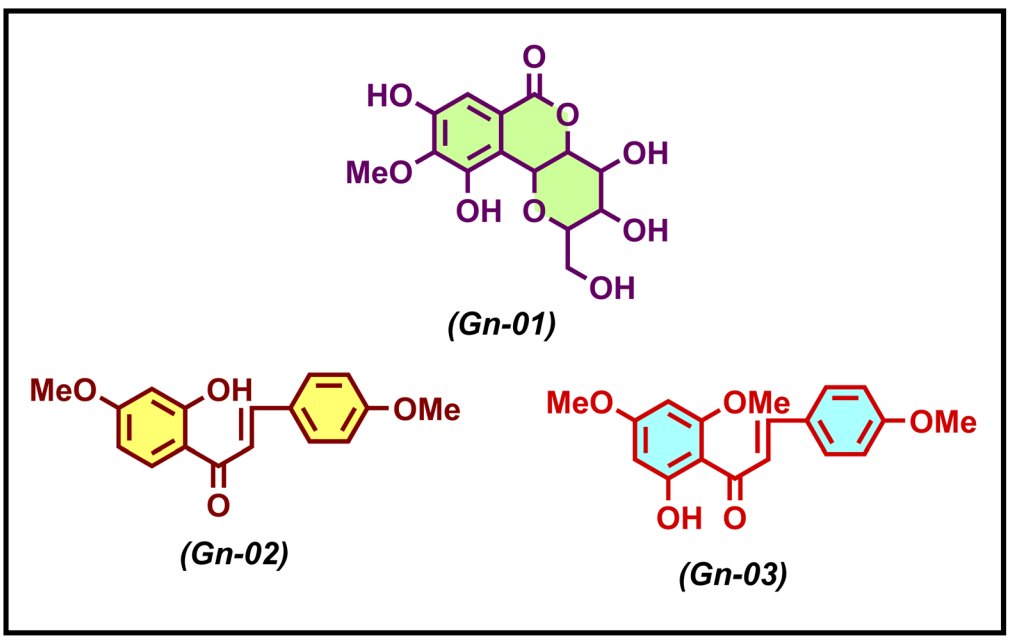

Fig. 1 Structure of three isolated compounds from the *Garcinia nervosa* plant leaves.

developing sensor-based diagnostic tools or therapeutic agents aimed at conditions associated with metal imbalances, such as Alzheimer's disease and other neurodegenerative disorders. Although *Gn*-01 (bergenin), a known phytochemical, is established for the first time with antioxidant and protein-binding activities, and chemotaxonomic significance to the genus. Beyond isolation, this work delivers an integrated structural functional profile, combining single-crystal X-ray diffraction and Hirshfeld surface analysis with antioxidant, HSA-binding, docking validation, and a novel demonstration of selective Cu^{2+} sensing *via* a fluorescence turn-on (CHEF) effect. This multidimensional approach provides a fresh perspective on a well-known compound, extending its potential applications into biosensing and diagnostics. Given these findings, *G. nervosa* emerges as a promising source for drug discovery, warranting extensive pharmacological and biochemical studies to explore its medicinal applications, including anti-inflammatory, anticancer, neuroprotective, and metal ion-related therapeutic potential.[22,27] Importantly, *Gn*-03 is isolated in a minimal quantity (15 mg); therefore, only structural characterization is reported in this work. Comprehensive *in vitro* bioassays for *Gn*-03 will be addressed in future studies through larger-scale isolation or synthetic/semi-synthetic approaches to enable biological evaluation.

2. Materials and methods

2.1. General experimental procedure

Using a Kofler apparatus, the compound's melting points were determined and reported without any modifications. The Thermo Scientific FLASH 2000 CHN Elemental Analyzer was used to perform elemental analyses for carbon, hydrogen, and nitrogen. The KBr pellet method was used to obtain FT-IR spectra on a PerkinElmer 2000 FTIR Spectrometer, and the findings were displayed in cm^{-1}. A PerkinElmer UV WinLab spectrophotometer was used to record the UV spectra. Using $CDCl_3$ as the solvent, proton (^1H) and carbon (^{13}C) NMR spectra were obtained using a Bruker Avance II instrument running at 400 MHz and 100 MHz, respectively. The coupling constants (J) were represented in Hertz, and chemical shifts (δ) were supplied in ppm with reference to tetramethyl silane (TMS). A JEOL-D300 mass spectrometer was used to measure the mass spectra. Thin-layer chromatography (TLC) on silica gel G254-coated plates (20 × 5 cm and 50 × 10 cm, E-Merck) and iodine vapor detection was used to verify the purity of the fractions and compounds.

2.2. Plant materials

Professor Wazahat Husain of the Department of Botany at AMU, Aligarh, identified the *Garcinia nervosa* leaves former colleagues from Zaria, Nigeria, had collected. At AMU, Aligarh, a voucher specimen (WLH/20250/21-22) has been saved in the Department of Botany's herbarium.

2.3. Extraction and isolation

2.0 kg of the air-dried leaves were ground into a powder and then extracted thoroughly using 95% ethanol under reflux. Following filtration, a crude extract was obtained by evaporating the filtrate at a lowered pressure. After that, this extract was successively fractionated using petroleum ether, benzene, chloroform, acetone, ethyl acetate, and methanol. Thin-layer chromatography (TLC) analysis showed that the benzene and ethyl acetate fractions behaved similarly, and both tested positive for phenolic hydroxyl groups (using the ferric chloride test) and flavonoids (using Shinoda's test). Therefore, these fractions were combined. The resulting mixture of petrol and benzene extract was then subjected to silica gel column chromatography, with stepwise elution using a benzene-ethyl acetate mixture (1 : 0, 9 : 1 → 1 : 9), leading to the isolation of compound *Gn*-01. Further elution with a benzene-chloroform mixture (1 : 0, 9 : 1 → 1 : 9) resulted in the isolation of compounds *Gn*-02 and *Gn*-03. The purified compounds were obtained after multiple rounds of column chromatography and crystallization.

2.4. Spectral analysis of isolated compounds

2.4.1. 3,4,8,10-Tetrahydroxy-2-(hydroxymethyl)-9-methoxy-3,4,4*a*,10*b*-tetrahydropyrano[3,2-*c*]iso chromen-6(2*H*)-one (*Gn*-01). Chemical formula: $C_{14}H_{16}O_9$, mol. weight: 328, white crystals, recrystallized in MeOH, M.P., 237 °C, UV (DMSO) λ_{max} (nm): 246 and 280. Yield: 60 mg, IR (KBr) ν_{max} (cm^{-1}): 3398, 2958, 1692, 1630 and 1465, 1236, 1095 and 840. ^1H NMR (400 MHz, DMSO-d_6) δ: 6.96 (1H, m, Ar, 7-H); 5.7 (1H, d, H-10*b*); 4.97 (1H, dd, H-4*a*); 4.00 (1H, dd, H-4); 3.82 (2H, d, H-11); 3.78 (3H, s, H-12); 3.65 (1H, m, H-2); 3.50 (1H, dd, H-3). ^{13}C NMR (100 MHz, DMSO-d_6): δ 162.5 (C-6); 151.5 (C-8); 148.0 (C-10); 142.2 (C-9); 118.0 (C-6*a*); 117.1 (C-10*a*); 110 (C-7); 71.5 (C-2); 81.2 (C4*a*); 74.5 (C-4); 82.5 (C-10*b*); 72.3 (C-3); 61.0 (C-11); 60 (C-12). Elem. anal. calcd: C, 51.22; H, 4.91; O, 43.86. Found: C, 52.14; H, 5.10; O, 42.10.

2.4.2. (*E*)-1-(2-Hydroxy-4-methoxyphenyl)-3-(4 methoxyphenyl)prop-2-en-1-one (*Gn*-02). Chemical formula: $C_{17}H_{16}O_4$, mol. weight: 284, white crystals, recrystallized in MeOH, M.P. 85 °C. yield; 20 mg. IR (KBr) ν_{max} (cm^{-1}): 3280, 2871, 1675, 1605 and 1450, 1225. ^1H NMR (DMSO) δ: 13.56 (s, 1H), 7.8 (d, J = 9.4 Hz, 1H), 7.6 (d, J = 8.8 Hz, 2H), 7.4 (s, 1H), 7.3 (s, 1H), 6.9 (d, J = 8.8 Hz, 2H), 6.60 (dd, J = 9.0, 2.5 Hz, 1H), 6.0 (d, J = 2.5 Hz, 1H), 3.83 (d, J = 8.1 Hz, 6H). ^{13}C NMR (DMSO) δ: 192.08, 167.08, 166.03, 160.00, 145.08, 131.02, 130.2, 127.50, 114.02, 112.06, 113.09, 112.6, 101.0, 55.87, 55.55. Elem. anal. calcd: C, 71.82; H, 5.67; O, 22.51. Found: C, 71.14; H, 5.69; O, 23.10.

2.4.3. (*E*)-1-(2-Hydroxy-4,6-dimethoxyphenyl)-3-(4-methoxyphenyl)prop-2-en-1-one (*Gn*-03). Chemical formula: $C_{18}H_{18}O_5$, mol. weight: 314, pale yellow crystals, recrystallized in MeOH, M.P. 237 °C, UV (DMSO) λ_{max} (nm): 246 and 280, M.P. 114 °C, yield; 15 mg. IR (KBr) ν_{max} (cm^{-1}): 3378, 2905, 1630, 1570 and 1465, 1205. ^1H NMR (DMSO) δ: 14.25 (s, 1H), 7.80 (d, J = 8.7 Hz, 2H), 7.5 (d, J = 16.1 Hz, 1H), 7.3 (d, J = 8.8 Hz, 2H), 6.90 (d, J = 16.1 Hz, 1H), 6.1–5.9 (m, 2H), 3.80 (s, 3H), 3.72 (s, 6H). ^{13}C NMR (DMSO) δ: 192.92, 162.25, 161.10, 157.92, 143.42, 129.50, 128.10, 127.75, 128.35, 124.73, 114.73, 112.15, 93.62, 90.36, 90.97, 55.72. Anal. elem. anal.: C, 68.78; H, 5.77; O, 25.45; found: C, 67.47; H, 6.00; O, 24.92.

2.5. Antioxidant activity: radical scavenging activity

The antioxidant activity of *Garcinia nervosa* extract was assessed utilizing the DPPH (2,2-diphenyl-1-picrylhydrazyl) free radical scavenging assay, employing a refined protocol adapted from Braca group.[39–41] This method enabled a comparative analysis of the extract's scavenging efficiency against the standard antioxidant, ascorbic acid. 0.4 mM DPPH solution was freshly prepared and stabilized for 60 minutes under dark, cool conditions to prevent degradation. To evaluate antioxidant efficacy, 3 mL of the prepared DPPH solution was mixed with 1 mL of either ascorbic acid or the ethanolic extract of *Gn*-01 at varying concentrations (12.5, 25, 50, 100, and 200 μg mL^{-1}). The mixtures were incubated in the dark to minimize photodegradation, and absorbance was recorded at 517 nm using a UV-vis spectrophotometer. Ascorbic acid served as the positive control for comparison. A reduction in absorbance corresponded to an increase in free radical scavenging activity and was visually evident by the DPPH solution transitioning from purple to yellow, reflecting the decolorization process. The percentage of radical scavenging activity (RSA%) was quantified using the equation:

$$\text{Radicals scavenging activity } I(\%) = \left(\frac{A_0 - A_S}{A_0}\right) \times 100$$

where A_0 represents the absorbance of the DPPH radical (without the test sample). A_S represents the absorption of the DPPH radical in the various extract samples at different concentrations.

The RSA% was plotted against the logarithmic concentration, and IC_{50} values (concentration required to inhibit 50% of DPPH radicals) were determined *via* linear regression. Lower IC_{50} values, expressed in μg mL^{-1}, correlate with higher antioxidant activity. In this study, compound *Gn*-01 from *Garcinia nervosa* exhibited the strongest antioxidant activity, with an IC_{50} of 23.438 μg mL^{-1}, closely comparable to ascorbic acid (19.712 μg mL^{-1}). These findings highlight compound *Gn*-01 's potent free radical scavenging properties, suggesting its potential as a natural antioxidant for pharmacological applications.

2.6. Preparation of solution for protein binding assays

A modified version of an established method was used to investigate the interaction of the isolated compound with human serum albumin (HSA, purchased from Sigma-Aldrich, USA). To prepare a 10 μM HSA solution, 66.394 mg of HSA was dissolved in phosphate-buffered saline (PBS). The wavelength range for the measurements was set from 300 nm to 600 nm.

2.7. Fluorescence intensity and UV absorbance

Fluorescence and UV-visible absorption spectroscopy were utilized to investigate the interaction of compound *Gn*-01 with biomacromolecules, employing advanced methodologies in line with recent studies. Fluorescence measurements were performed using a spectrofluorometer (SpectraMax iD3) with excitation and emission slit widths set at 10 nm. An excitation wavelength of 280 nm was used for fluorescence emission, with emission spectra recorded between 300 and 600 nm. For UV absorbance, the spectra were collected in the 230 to 530 nm range. Data analysis and visualization were performed using OriginPro and Microsoft excel, enabling the generation of regression plots and comprehensive data modeling. The interaction parameters were quantified using the Stern–Volmer equation (eqn (i)) and the modified Stern–Volmer equation (eqn (ii)). These equations facilitated the calculation of key parameters, consisting of the number of binding sites (n), the binding constant (K_b), and the Stern–Volmer quenching constant (K_{sv}). Using eqn (ii), the quenching rate constant (K_q) was calculated. The average fluorescence lifespan of the proteins without the quencher, denoted by τ_0, was found to be 10^{-9} s.[39,42]

$$F_0/F = 1 + K_{sv}[Q] \quad \text{(i)}$$

$$\log(F_0 - F)/F = \log K_b + n \log[Q] \quad \text{(ii)}$$

$$K_q = K_{sv}/\tau_0 \quad \text{(iii)}$$

2.8. KI quenching studies

Iodide quenching tests were carried out alongside and without human serum albumin (HSA). *Gn*-01 compounds were dissolved in 10 mM Tris–HCl buffer (pH 7.2) and titrated with 0–10 μM potassium iodide (KI).[43] Fluorescence measurements were taken by exciting the compounds at 280 nm, and the emission spectra were recorded between 300 and 400 nm. In a separate set of experiments, a mixture of compounds *Gn*-01 (10 μM) and HSA (10 μM) was prepared, followed by the addition of KI in varying concentrations (0–10 mM). The Stern–Volmer equation was employed to determine the quenching constant (K_{sv}) in both conditions, with and without HSA.

2.9. Circular dichroism spectroscopy

Using a Jasco J-815 Circular Dichroism (CD) spectropolarimeter, alterations in the secondary (α-helical and β-sheet) and tertiary structures of HSA upon binding contacts were examined under controlled conditions at 298.15 K. Spectra were acquired using a high-precision 1 mm path-length quartz cuvette, with measurements conducted at a scan rate of 100 nm min^{-1} and a sensitivity setting of 100 mdeg. The instrument parameters were optimized for high-resolution data acquisition, employing a response time of 2 sec and a bandwidth of 0.2 nm to ensure an accurate assessment of structural changes in the protein conformations.

2.10. Crystal structure determination, molecular docking, and Hirshfeld surface studies

Single-crystal X-ray diffraction determined the structure of $C_{14}H_{16}O_9$, which crystallizes in the orthorhombic space group $P2_12_12_1$ at 293 K. Unit cell parameters are a = 7.4995 (5) Å, b = 13.933 (2) Å, and c = 14.2792 (10) Å. Mo-Kα radiation (λ = 0.71073 Å) was used. 21 880 reflections were measured, yielding 3232 independent reflections (R_{int} = 0.043), with 2701

having $I > 2\sigma(I)$. The structure was solved and refined using SHELXL-2018/3, resulting in $R\,[F^2 > 2\sigma(F^2)] = 0.037$ and $wR\,(F^2) = 0.088$. The Flack parameter was −0.4 (5). Hirshfeld surface analysis was conducted to investigate the nature and extent of intermolecular interactions within the crystal structure. The analysis utilized CrystalExplorer software, with the X-ray single-crystal CIF file of the organic compound as the input. Hirshfeld surfaces and corresponding 2D fingerprint plots were generated to visualize and quantify these interactions. Hirshfeld surface analysis, using CrystalExplorer 21,[44,45] calculated the normalized contact distance (d_{norm}) to visualize and quantify intermolecular interactions. d_{norm} considers the distances (d_i, d_e) of closest atoms inside and outside the surface, adjusted by van der Waals radii. Molecular docking of the isolated compound *Gn*-01 against Human Serum Albumin (HSA, PDB ID: 1AO6) was performed using AutoDock Vina 1.1.2. The HSA structure was obtained from the Protein Data Bank.[46] Protein and ligand preparation were conducted using AutoDock Tools (ADT).[47,48] A grid box with dimensions of 30 Å along each axis and a grid spacing of 0.375 Å was centered at *X*: 27, *Y*: 23, *Z*: 23 to encompass the putative binding site. Following completion of the docking calculations, the top-ranked pose, exhibiting the lowest binding energy, was selected for visualization. Visualization and analysis were performed using BIOVIA Discovery Studio and PDBSum server.

2.11. Sample preparation

Stock solutions of metal chlorides, including Mn^{2+}, Fe^{2+}, Ni^{2+}, Cu^{2+}, and Zn^{2+}, were prepared in ethanol at an initial concentration of 1.0×10^{-3} mol L^{-1}. These stock solutions were subsequently diluted to a working concentration of 1.0×10^{-5} mol L^{-1} for spectral analysis. Similarly, a stock solution of the compound *Gn*-01 was prepared in DMSO at 1.0×10^{-3} mol L^{-1} and diluted to a final concentration of 1.0×10^{-5} mol L^{-1} to ensure consistency and compatibility in the spectroscopic evaluation.

2.12. Photophysical studies

Fluorescence and ultraviolet-visible spectroscopy were performed to investigate the chemo-sensing capabilities of compound *Gn*-01 in the presence of various metal ions within the DMSO solvent system. To optimize the sensitivity of the fluorescence measurements, a slit width of 10 nm was applied. Fluorescence spectra were acquired at excitation wavelengths of 372 nm, with emission monitoring across the relevant spectral range. These measurements were meticulously designed to explore the interaction dynamics between compound *Gn*-01 and metal ions, providing critical insights into its potential as a selective sensor. The combination of UV-vis absorption and fluorescence spectroscopy enabled a comprehensive analysis of the binding and interaction profiles, offering a detailed understanding of the compound's sensory response to metal coordination.

3. Result and discussion

3.1. Structural elucidation

Compound *Gn*-01 was obtained as a white crystalline material with a M.P. of 237 °C, aligning closely with the reported M.P. of *Gn*-01 (236 °C). The UV-vis spectrum of compound *Gn*-01 in DMSO exhibited characteristic absorption peaks at 246 nm and 280 nm (Fig. S1), showing a slight deviation from the theoretical values of bergenin due to the solvent effect of DMSO.[49–51] The FTIR spectrum identified key functional groups, including hydroxyl (3398 cm^{-1}), methyl (2958 cm^{-1}), carbonyl (1692 cm^{-1}), benzene ring (1630 and 1465 cm^{-1}), C–O stretching of the methoxy group (1236 cm^{-1}), and substituted phenolic groups (1095 and 840 cm^{-1}) (Fig. S2). The ^{1}H NMR spectrum exhibited a singlet at δ 6.96, attributed to an aromatic proton, and another singlet at δ 3.78 for the methoxy protons (3H) (Fig. S3). The ^{13}C NMR spectrum revealed signals for fourteen carbons, including a carbonyl carbon at δ 162.5, a methoxy carbon at δ 60, and olefinic carbons at δ 162.50, 118.00, 110.00,

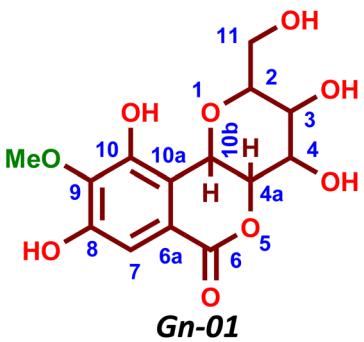

Fig. 2 Structure of isolated compound 3,4,8,10-tetrahydroxy-2-(hydroxymethyl)-9-methoxy-3,4,4*a*,10*b*-tetrahydropyrano[3,2-*c*]isochromen-6(2*H*)-one (Bergenin).

Table 1 ^{1}H NMR and ^{13}C NMR spectral data of isolated compound *Gn*-01 (Bergenin)

Position	^{1}H NMR	^{13}C NMR	Position	^{1}H NMR	^{13}C NMR
2	3.65 (1H, m, H-2)	71.5	8	9.83 (OH)	151.5
3	3.50 (1H, dd, H-3)	72.3	9	—	142.2
4	4.00 (1H, dd, H-4)	74.5	10	8.40 (OH)	148.0
4*a*	4.97 (1H, dd, H-4*a*)	81.2	10a	—	117.1
5	—	—	10b	5.7 (1H, d, H-10*b*)	82.5
6	—	162.5	11	3.82 (2H, m)	61
6*a*	—	118.0	OCH_3	3.78 (3H, s, H-12)	60
7	6.96 (1H, m, H-7)	110	—	—	—

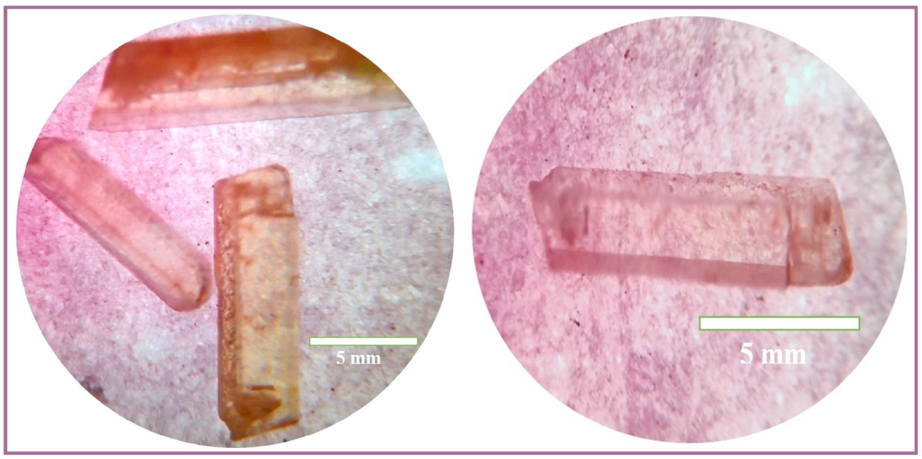

Fig. 3 Microscopic views of a single crystal of (*Gn*-01).

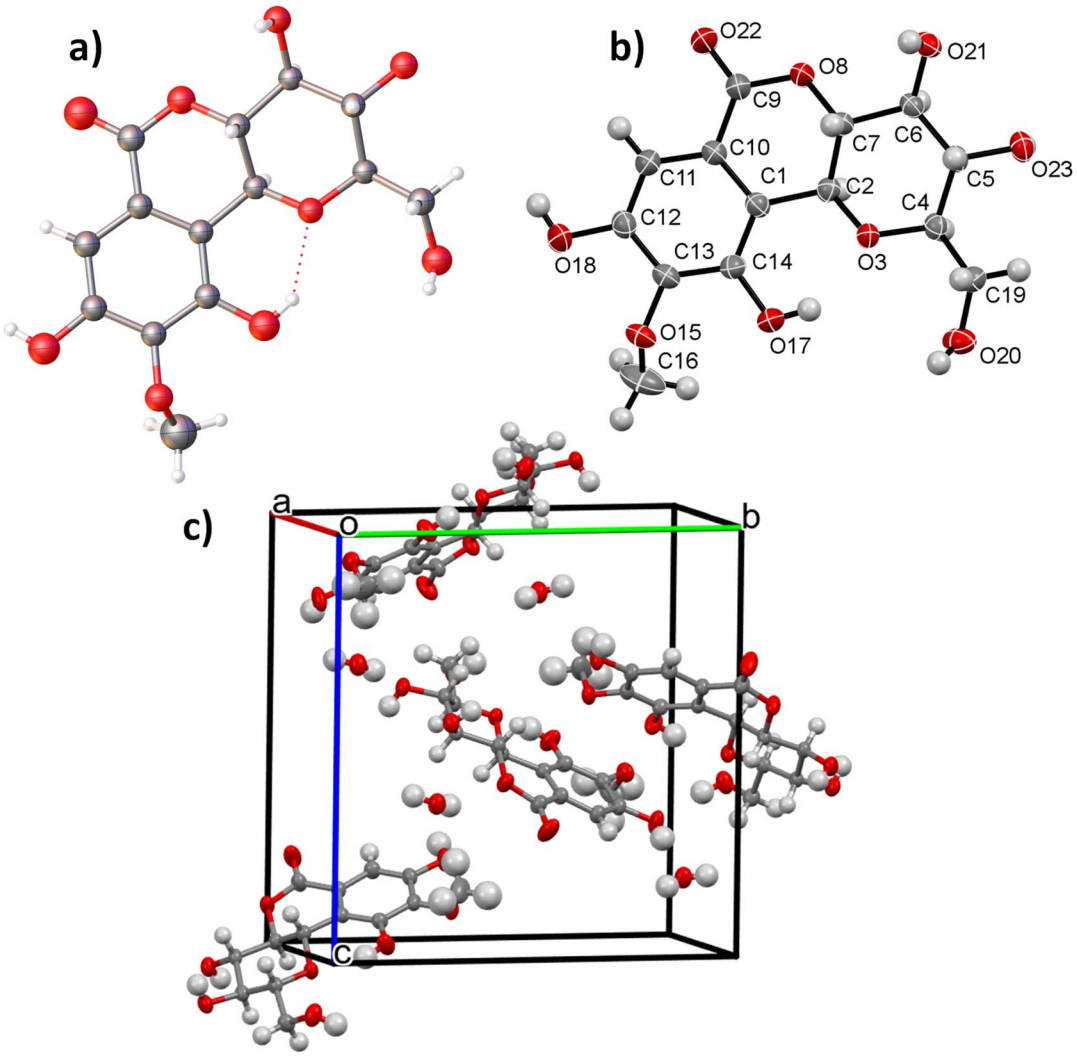

Fig. 4 (a) Ball-and-stick representation of (*Gn*-01) with atom labelling. Ellipsoids are shown at the 50% probability level (b) ORTEP-style representation, ellipsoids are displayed at the 50% probability level, and (c) crystal packing diagram along *a* axis showing the unit cell of (*Gn*-01). The unit cell contains four molecules ($Z = 4$) along with solvent molecules.

151.50, 142.20, 148.00, and 115.95 (Fig. S4). A comparative analysis of these spectral data with previously published literature confirmed that the structure of *Gn*-01 is a bergenin (Table 1), as shown in Fig. 2, identified as 3,4,8,10-tetrahydroxy-2-(hydroxymethyl)-9-methoxy-3,4,4*a*,10*b*-tetrahydropyrano[3,2-*c*] isochromen-6(2*H*)-one, supported by single-crystal X-ray diffraction analysis in the present work. Additional 2D NMR data (HSQC, HMBC, COSY) were acquired to support the structural assignment, and the corresponding spectra are provided in the SI Fig. S5.

3.2. Crystal structure determination of compound (*Gn*-01)

The microscopic single-crystal images reveal a prismatic morphology with well-defined elongated rectangular faces, sharp edges, and a columnar growth pattern, suggesting a preference for directional molecular packing. The absence of globular or dendritic growth structures indicates a well-defined prismatic habit, typically observed in monoclinic and orthorhombic systems. By estimating the crystal dimensions using the 5 mm scale bar, the approximate sizes are single crystal (~10 mm length × ~1.2 mm width × ~1 mm thickness) (Fig. 3). These dimensions indicate a high aspect ratio, a feature common in orthorhombic organic crystals due to anisotropic growth conditions, influenced by intermolecular interactions, solvent effects, and crystallization kinetics. The single-crystal X-ray diffraction (SCXRD) analysis confirms that the obtained organic crystals exhibit an orthorhombic crystal system, characterized by three mutually perpendicular axes of unequal lengths. This morphology aligns with literature reports on prismatic organic single crystals, known for their stability, mechanical robustness, and anisotropic optical properties, making them valuable for organic electronics, pharmaceuticals, and nonlinear optics.

3.2.1 SC X-ray diffraction analysis of compound *Gn*-01. For the first time, the crystal structure of *Gn*-01 (bergenin) isolated from *Garcinia nervosa* has been elucidated by single-crystal X-ray diffraction (CCDC 2427544). The molecule crystallizes in a well-ordered lattice stabilized predominantly by an extensive O–H···O hydrogen-bonding network, which links adjacent molecules into a robust supramolecular framework (Fig. 4). Hirshfeld surface analysis further revealed that these O–H···O interactions, together with significant H···H contacts and additional weaker C–H···O/C···O contributions, dominate the intermolecular packing forces (Fig. 5). The visualization of these interactions highlights the balance of strong directional hydrogen bonds with weaker van der Waals contacts, collectively ensuring structural stability. Symmetry operations confirm that the molecules are arranged in a centrosymmetric fashion, generating repeating hydrogen-bonded motifs that extend throughout the lattice and reinforce the supramolecular assembly. Beyond confirming the molecular identity, this structural insight provides valuable chemotaxonomic information and establishes a solid-state basis for interpreting the biological and photophysical behavior of *Gn*-01. For completeness, the full crystallographic dataset, including unit cell parameters, refinement details, bond lengths and angles, packing diagrams, and comprehensive Hirshfeld fingerprint plots, is provided in the SI (Tables S1–S3).

3.3. Hirshfeld surface analysis

Hirshfeld surface analysis of compound *Gn*-01 was functioned to understand its intermolecular interactions using CrystalExplorer 21. The d_{norm}-mapped surface (Fig. 6a) shows significant intermolecular interactions, with red areas indicating tight contacts, mainly corresponding to strong O–H···O hydrogen bonds. These interactions play a crucial role in stabilizing the crystal structure. In addition, the shape index mapped surface (Fig. 6b) highlights possible π-stacking or other close contact interactions, represented by alternating red (convex) and blue (concave) regions.

The fingerprint map representing all intermolecular interactions (Fig. 6c) provides a comprehensive view of the contact

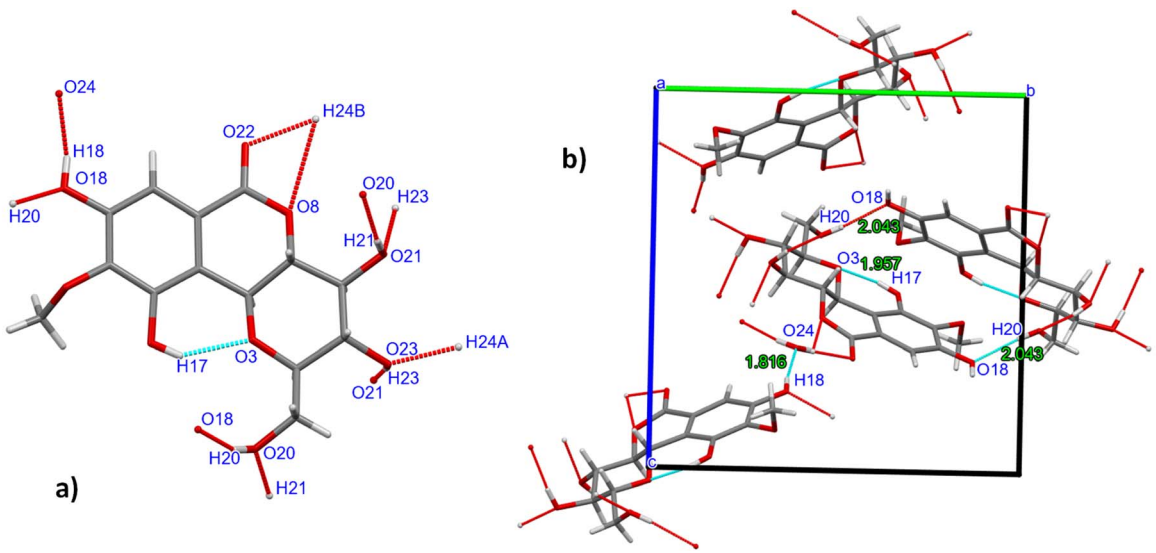

Fig. 5 (a) The dominant C–H···O hydrogen bonds found in the crystal of *Gn*-01, (b) molecular packing of the unit cell of compound (*Gn*-01).

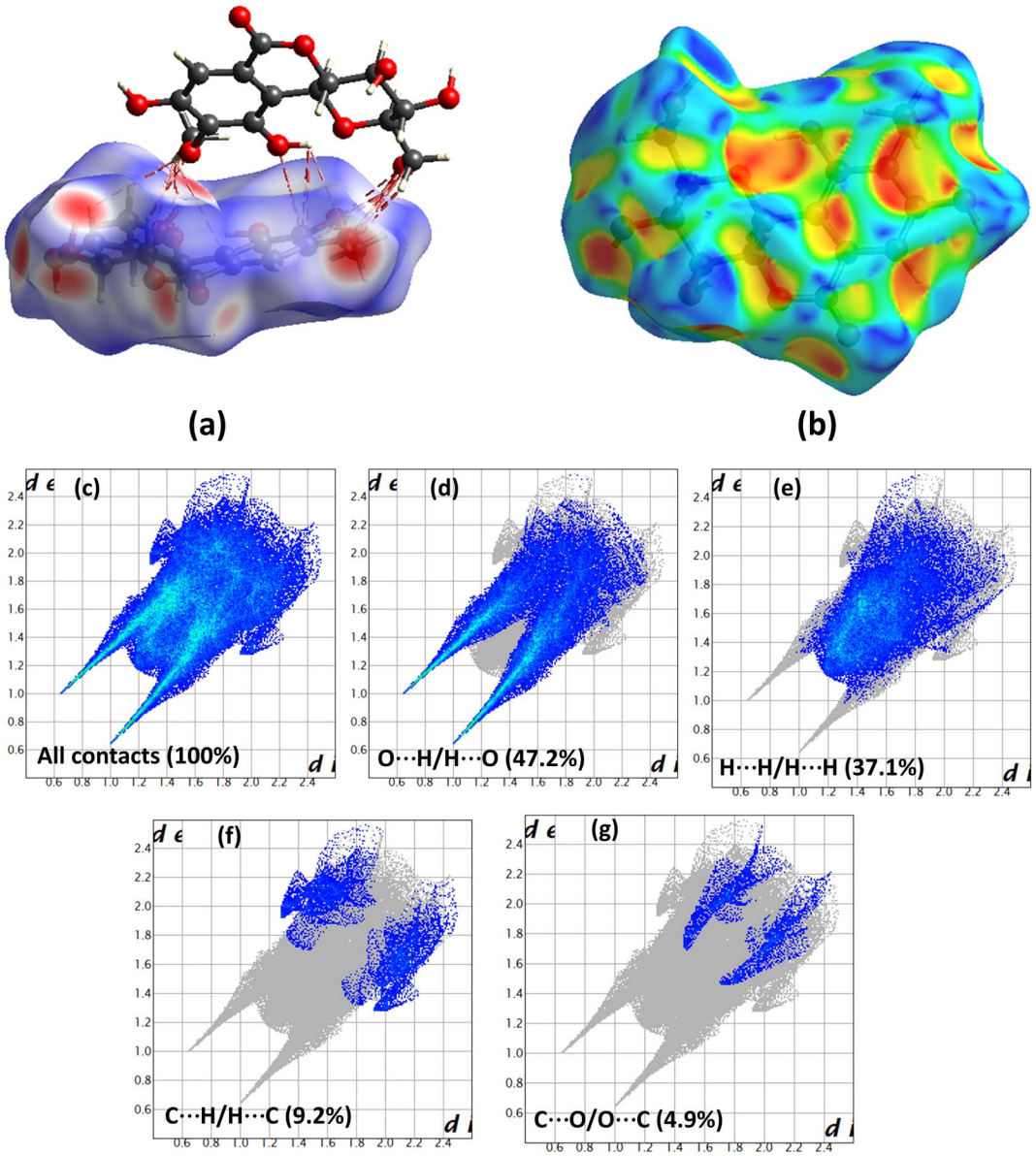

Fig. 6 Hirshfeld surface analysis of compound *Gn*-01. (a) d_{norm}-mapped Hirshfeld surface illustrating intermolecular interactions. Red regions indicate tight contacts, particularly those associated with O–H···O hydrogen bonds. (b) Shape index-mapped Hirshfeld surface highlighting potential π-stacking or other close contacts interactions through adjacent red (convex) and blue (concave) regions. (c) Full fingerprint depicting all intermolecular contacts. (d–g) Decomposed fingerprints showing specific contact contributions: (d) O–O···H/H···O (47.2%), (e) H···H (37.1%), (f) C···H/H···C (9.2%), and (g) C···O/O···C (4.9%). d_i and d_e represent the distance from the surface to the nearest atom inside and outside the Hirshfeld surface, respectively.

contributions. Decomposition of the fingerprint map allows for quantitative analysis of specific intermolecular interactions. The most important contribution comes from the O···H/H···O interactions, which account for 47.2% of the total Hirshfeld surface (Fig. 6d). This dominance is expected because hydroxyl and oxygen-containing groups promote strong hydrogen bonds. The second most prominent interaction type is H···H contacts, which account for 37.1% of the total surface (Fig. 6e). Although weaker than hydrogen bonds, these interactions play a role in crystal packing stability through van der Waals forces. Carbon-related interactions, including C···H/H···C contacts, contribute 9.2% (Fig. 6f). These contacts may indicate weak C–H···π interactions, which facilitate molecular organization within the lattice. Finally, C···O/O···C interactions account for 4.9% of the total surface (Fig. 6g), indicating weak dipole interactions between carbonyls and other oxygen-containing functional groups. Overall, the Hirshfeld surface analysis provides a detailed understanding of the intermolecular forces governing the crystal packing of compound *Gn*-01. The dominant role of O···H/H···O hydrogen bonds suggests a significant contribution to structural stability, while weaker van der Waals and π-related interactions further reinforce the packing arrangement. These insights highlight the importance of hydrogen-bonding

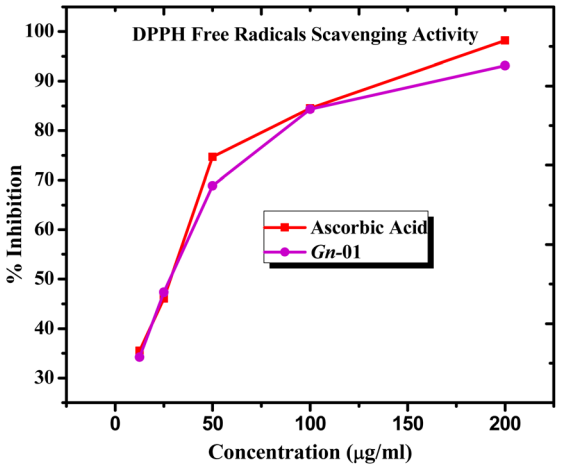

Fig. 7 DPPH free radical scavenging activity of compounds *Gn*-01 as compared to ascorbic acid.

networks in determining the solid-state properties of compound *Gn*-01.

3.4. Antioxidant activity analysis

The IC_{50} value, representing the concentration required to achieve 50% inhibition of free radicals, was determined using linear regression analysis (Fig. 7). This analysis correlates scavenging activity (%) or inhibition (%) with the logarithmic concentration of the sample. A lower IC50 signifies a greater antioxidant capacity. *Gn*-01 demonstrated the highest antioxidant potential among the tested compounds, with an IC_{50} value of 23.438 μg mL^{-1}. *Gn*-01 Antioxidant activity is categorized as strong for IC_{50} values between 10 and 50 μg mL^{-1}, and intermediate for values ranging from 50 to 100 μg mL^{-1}. Accordingly, compound *Gn*-01 exhibits robust antioxidant properties.

3.5. UV visible spectroscopy

UV-visible spectroscopy is a well-established technique for investigating the interaction between small molecules and biomacromolecules such as human serum albumin (HSA). In this study, the absorption spectra of compound *Gn*-01 revealed two characteristic absorption maxima at 246 nm and 280 nm. A hyperchromic effect was observed upon the incremental addition of HSA (Fig. 8), indicating an increase in absorbance intensity. The occurrence of hyperchromic in such interactions is typically associated with non-covalent external binding, suggesting that compound *Gn*-01 interacts with HSA *via* surface-accessible pocket rather than deeply embedding within the protein.

To further evaluate the binding strength of compound *Gn*-01 with HSA, the intrinsic binding constant ($K_b \approx 3.56 \times 10^4$ M^{-1}) was determined using the Benesi–Hildebrand equation. A double reciprocal plot of $1/(A - A_0)$ *versus* 1/[HSA] yielded a linear relationship, confirming the formation of a stable complex. The estimated binding constant (K_b) for compound *Gn*-01 was found to be in the order of 10^4 M^{-1}, further supporting its non-intercalative binding dynamic quenching mode with HSA. These findings reveal significant insight into the molecular interaction mechanism between compound *Gn*-01 and HSA, which is vital to recognizing its binding affinity, pharmacokinetic behavior, and prospective biological applications.

3.6. Fluorescence quenching

Fluorescence spectroscopy investigated the interaction between compound *Gn*-01 and human serum albumin (HSA). A notable quenching effect was observed in the fluorescence intensity of compound *Gn*-01 upon the incremental addition of HSA (Fig. 9), indicating a direct interaction between the molecules. To further quantify this interaction, the fluorescence intensity ratio (F_0/F) was plotted as a function of HSA concentration, and the Stern–Volmer quenching constant (K_{SV}) was determined from the slope. The calculated K_{SV} value for compound *Gn*-01 was 168.3×10^4 M^{-1}, which is lower than that of classical intercalators, suggesting a non-intercalative binding mode with HSA, and the rate constant K_q is 1.68×10^{12} M^{-1} s^{-1} (Table 2). The higher K_{sv} value is likely related to the strong polarity-

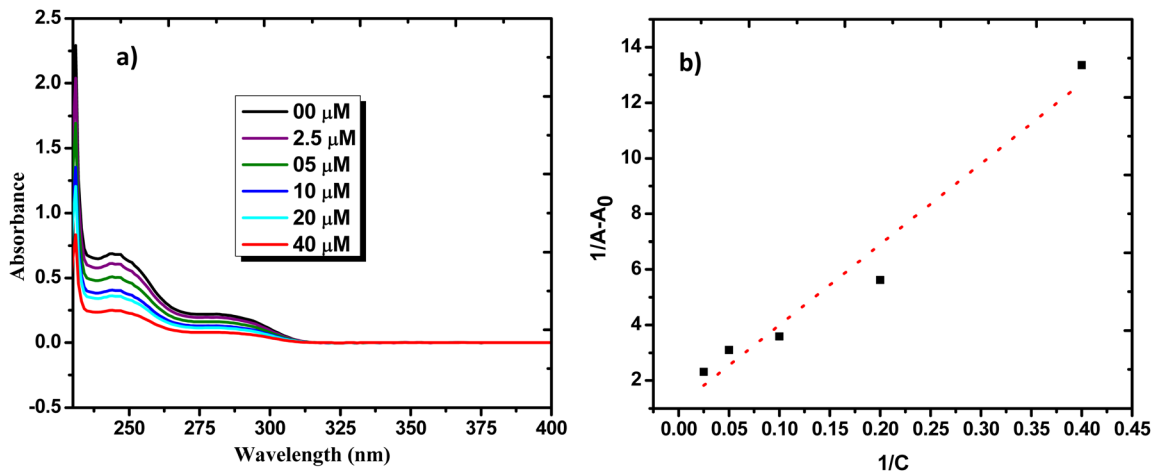

Fig. 8 Interaction of compound *Gn*-01 with HSA: (a) UV-visible absorption spectra of *Gn*-01 (5 μM) recorded at concentrations of HSA (0–40 μM) in Tris–HCl buffer (pH 7.2); (b) corresponding inverse plot of *Gn*-01.

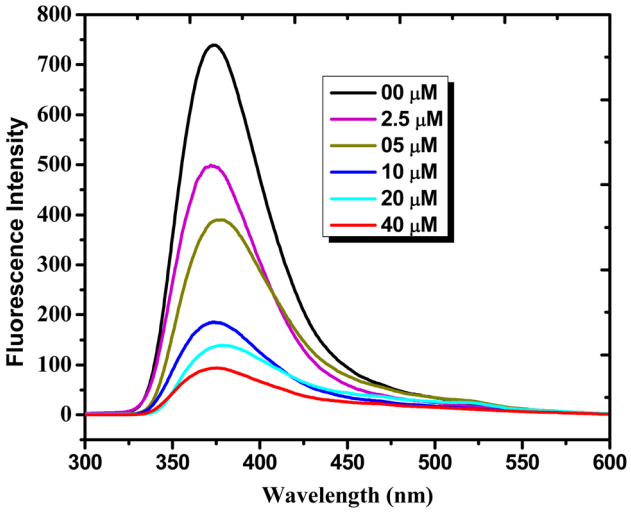

Fig. 9 Fluorescence emission spectra of compound *Gn*-01 (10 μM) with increasing concentrations of HSA (0–40 μM).

sensitive fluorescence response of *Gn*-01 within the HSA binding site, which contributes to an elevated apparent quenching constant.

Furthermore, using the modified Stern–Volmer equation, the binding constant (K_b) and binding stoichiometry (n) of the compound-HSA complex were calculated using fluorescence spectrum data. The binding constant (K_b) of compound *Gn*-01 with HSA was determined to be 3.16×10^4 M^{-1}, with a binding stoichiometry (n) of 0.98, as obtained from the $\log[(F_0 - F)/F]$ *vs.* log[HSA] plot. The linearity of the modified Stern–Volmer plots ($R^2 \approx 0.99$), Fig. 10b, further supports the accuracy of the binding analysis. These results collectively suggest that compound *Gn*-01 interacts with HSA through a non-intercalative, surface-accessible pocket, most likely within a drug-binding cavity, stabilized by hydrogen bonding and hydrophobic interactions. This study provides valuable insights into the molecular binding characteristics of compound *Gn*-01 with HSA, contributing to a deeper understanding of its pharmacokinetic behavior and biological significance.

3.7. Circular dichroism spectra

Circular dichroism (CD) spectroscopy is an effective method for assessing conformational changes in proteins. Non-covalent interactions between proteins and small molecules can modify the intrinsic CD spectra, particularly affecting the α-helical structure.[52] In the presence of compound *Gn*-01, a reduction in the intensity of the characteristic α-helix peaks at 208 nm and 222 nm was observed, suggesting a decrease in α-helical content (Fig. 11). This indicates that compound *Gn*-01 may induce partial unfolding or alter the secondary structure of

Table 2 Fluorescence data were used to determine the following parameters

Replicate Stern–Volmer and binding parameters for *Gn*-01 with HSA

Replicate	K_{sv} ($\times 10^4$ M^{-1})	K_q ($\times 10^{12}$ M^{-1} s^{-1})	K_b ($\times 10^4$ M^{-1})	n (binding sites)	R^2
1	168.4	1.68	3.21	0.98	0.992
2	167.5	1.68	3.09	0.97	0.989
3	169.1	1.69	3.18	0.99	0.991
Mean ± SD	168.3 ± 0.8	1.68 ± 0.01	3.16 ± 0.06	0.98 ± 0.01	0.991 ± 0.001

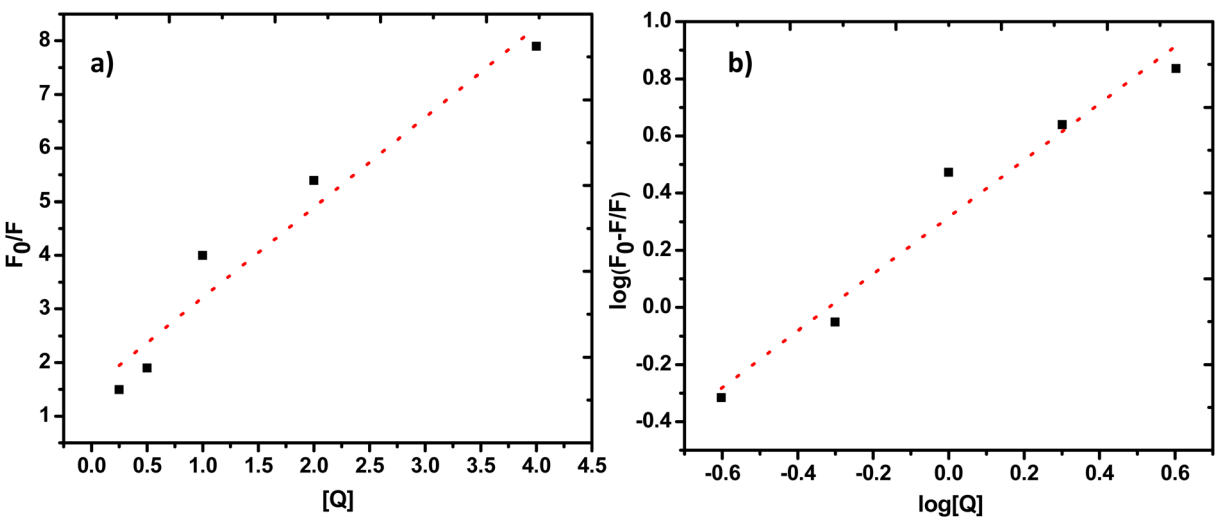

Fig. 10 (a) Stern–Volmer plot and (b) modified Stern–Volmer plot for HSA, illustrating the quenching effect of compound *Gn*-01 through F_0/F *vs.* [Q] and $\log(F_0 - F)/F$ *vs.* log[Q].

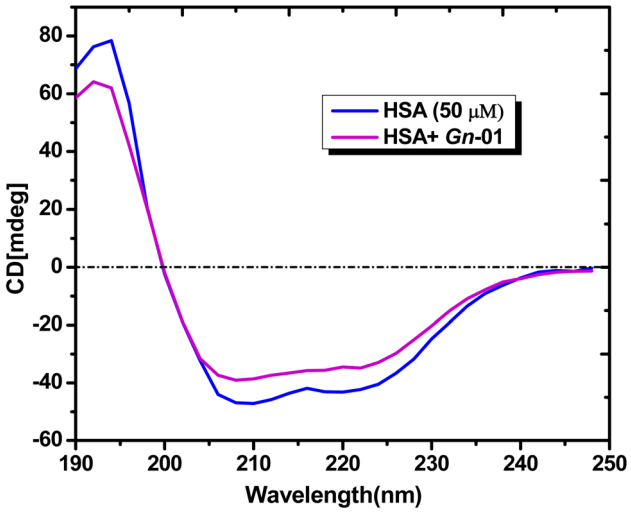

Fig. 11 UV-CD spectra of protein HSA and their interaction with compound *Gn*-01.

the protein. Interestingly, while the alpha-helicity slightly increased upon interaction with *Gn*-01, no significant shift in the peak position was detected, supporting a non-intercalative mode of interaction. Further fluorescence spectroscopy studies would provide deeper insights into the binding mechanisms and interaction strength.

3.8. KI quenching studies

The iodide quenching assay serves as a valuable tool for investigating the binding interactions between small molecules and human serum albumin (HSA) by assessing fluorescence quenching behavior. This technique exploits the principle that when a molecule is intercalated within the HSA structure, it is shielded from external quenchers due to electrostatic repulsion by negatively charged protein regions. Consequently, its fluorescence remains largely unaffected in the presence of iodide ions. Conversely, surface-bound molecules remain exposed on the protein surface, allowing direct interaction with quenchers and leading to significant fluorescence quenching even in the presence of HSA (Fig. 12). To quantify this interaction, fluorescence quenching data were analyzed using the Stern–Volmer equation.

In this study, the quenching constant K_{sv} of the compound *Gn*-01 was found to be 0.59×10^4 M^{-1} in the absence of HSA, which increased significantly to 4.521×10^4 M^{-1} in the presence of HSA (Fig. 13). This marked increase suggests that the molecule remains exposed to the quencher even after binding to HSA, ruling out intercalation. Instead, this behavior is characteristic of groove binding or electrostatic surface interactions, where the compound remains externally associated with the protein, allowing easy access to iodide ions. Thus, the quenching analysis confirms that the compound *Gn*-01 exhibits a non-intercalative binding mode with HSA, favouring groove binding or an external electrostatic interaction rather than internal embedding within the protein structure. This finding provides valuable insight into the molecular interaction of the compound with serum albumin, which is essential for understanding its pharmacokinetics and potential biological applications.

3.9. Molecular docking analysis

To understand the molecular interactions of (3,4,8,10-tetrahydroxy-2-(hydroxymethyl)-9-methoxy-3,4,4*a*,10*b*-tetrahydropyrano[3,2-*c*]isochromen-6(2*H*)-one) (compound *Gn*-01) with human serum albumin (HSA) (PDB ID: 1AO6), molecular docking was carried out using AutoDock Vina. The docking process involved preparing the HSA structure (Fig. 14a) and the ligand molecule (Fig. 14b) before performing docking simulations. The docking procedure placed the ligand within the active site of HSA (Fig. 14c), where it adopted an energetically favorable conformation. The best-docked pose exhibited a binding affinity of −7.364 kcal mol^{-1}, suggesting a significant interaction between the ligand and HSA. The binding mode analysis revealed that the ligand formed multiple interactions with key amino acid residues (Fig. 14d), including ARG145,

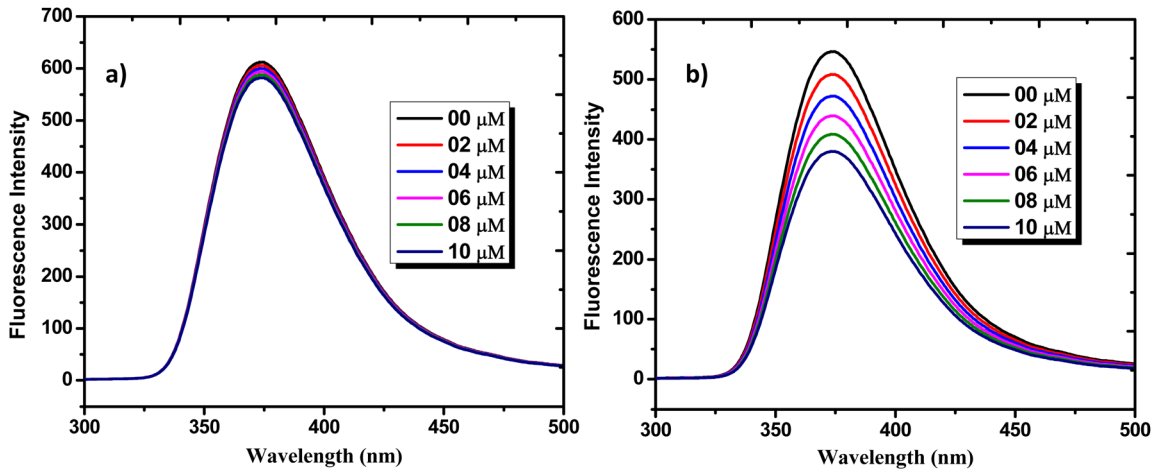

Fig. 12 The quenching of compound *Gn*-01 with KI fluorescence was recorded in (a) the absence and (b) the presence of HSA.

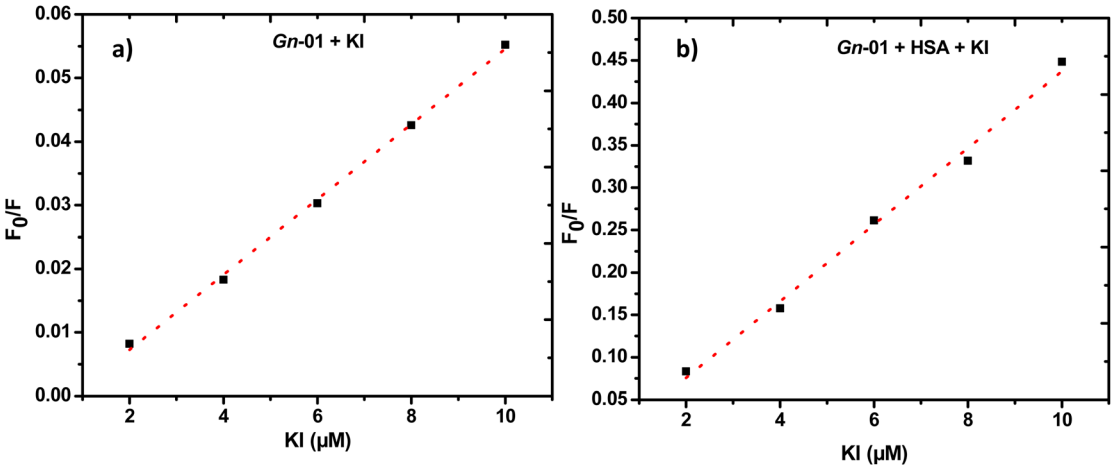

Fig. 13 Stern–Volmer plots representing the interaction of *Gn*-01 with KI (a) absence and (b) presence of HSA.

SER193, ARG197, ASN109, ASP108, ALA194, LYS190, GLN459, and GLU425. These interactions included conventional hydrogen bonds, specifically between ARG145, ASP108, and SER193, and compound *Gn*-01 in domain 1B, along with van der Waals forces and carbon–hydrogen bonds, contributing to the ligand's stability within the active site. Notably, ARG145, ASP108, and SER193 played significant roles in hydrogen bonding with the hydroxyl functional groups of the ligand (Fig. 14d). These residues, which participate in hydrogen bonding, collectively play a crucial role in ligand accommodation, specificity, and the overall structural stability of HSA's binding sites. A detailed visualization of the specific binding interactions is shown in Fig. 14e, where hydrogen bonding and hydrophobic interactions are highlighted. The ligand exhibits a substantial binding affinity towards HSA, suggesting potential impacts on its pharmacokinetics and bioavailability. Compound *Gn*-01 effectively binds within the HSA active site through a network of hydrogen bonds and hydrophobic interactions, potentially modulating HSA's affinity for endogenous ligands or drugs. This study provides a molecular understanding of the ligand–HSA complex, which is supported by our experimental findings from UV-visible and fluorescence spectroscopy. The experimentally determined binding constants ($K_b \approx 3.1$–3.5×10^4 M^{-1}; $K_{sv} \approx 1.68 \times 10^6$ M^{-1}) are in the typical range for HSA–ligand interactions, suggesting a consistent picture of moderate but stable binding through a non-intercalative mechanism. To investigate potential binding pockets and internal channels within Human Serum Albumin (HSA), MOLEonline 2.0, a web-based tool integrated into PDBsum, was employed to identify and characterize pores within the protein structure (Fig. 15). The analysis considered several key parameters, including radius-free (effective pore radius), '*R*-length (pore length), HPathy (hydrophilicity/hydrophobicity), HPhob' (hydrophobicity), polar (polarity), and Rel Mut (relative mutability). Pore 1 exhibited a 'radius-free' of 2.43 Å and an '*R*-length' of 63.1 Å, while Pore 2 had the same 'radius-free' but an extended '*R*-length' of 71.5 Å. The negative 'HPathy' values (−2.48 and −2.67) indicate a predominantly hydrophilic environment within both pores. This analysis was performed on the crystal structure of HSA (PDB ID: 1AO6) to identify internal spaces capable of accommodating compound *Gn*-01. The study focused on pores longer than 25 Å, as larger cavities (63.1 Å and 71.5 Å) are more likely to represent functional binding sites or transport pathways. To assess the impact of ligand binding on pore properties, the analysis was conducted both in the absence and presence of HETATM atoms (ligand 1), as illustrated in Fig. 15a and b. Additionally, an alternative pore representation is shown in Fig. 15c, where differences in cavity accessibility and ligand interaction are highlighted.

Further structural visions into the identified pores are provided in Fig. 15d, where the amino acid residues within these cavities are classified in detail. The residue distribution is categorized based on physicochemical properties, including positively charged (H, K, R), negatively charged (D, E), neutral (S, T, N, Q), aliphatic (A, V, L, I, M), aromatic (F, Y, W), proline/glycine (P, G), and cysteine (C) residues.

Analysis of the residue composition within the pores reveals distinct variations in the microenvironment of each cavity. Pore 1 is primarily enriched in positively charged residues (7 occurrences) and negatively charged residues (5 occurrences), as well as neutral (4) and aliphatic (4) residues. In contrast, pore 2 has a high occurrence of both positively charged (9) and negatively charged (8) residues, but a low number of aliphatic residues (2). Notably, no aromatic residues were detected in either pore, suggesting limited hydrophobic interactions in these regions. The presence of proline/glycine residues, although rare, may contribute to the structural flexibility of the pore-lining regions.

This residue-based classification provides valuable insights into the electrostatic and hydrophobic properties that govern ligand interactions within these pores. The predominance of charged residues suggests a possible role in selective ion transport or molecular recognition. Furthermore, differences in residue composition between pores suggest possible differences in binding affinity and accessibility to exomolecules. This analysis is critical to understanding the functional significance

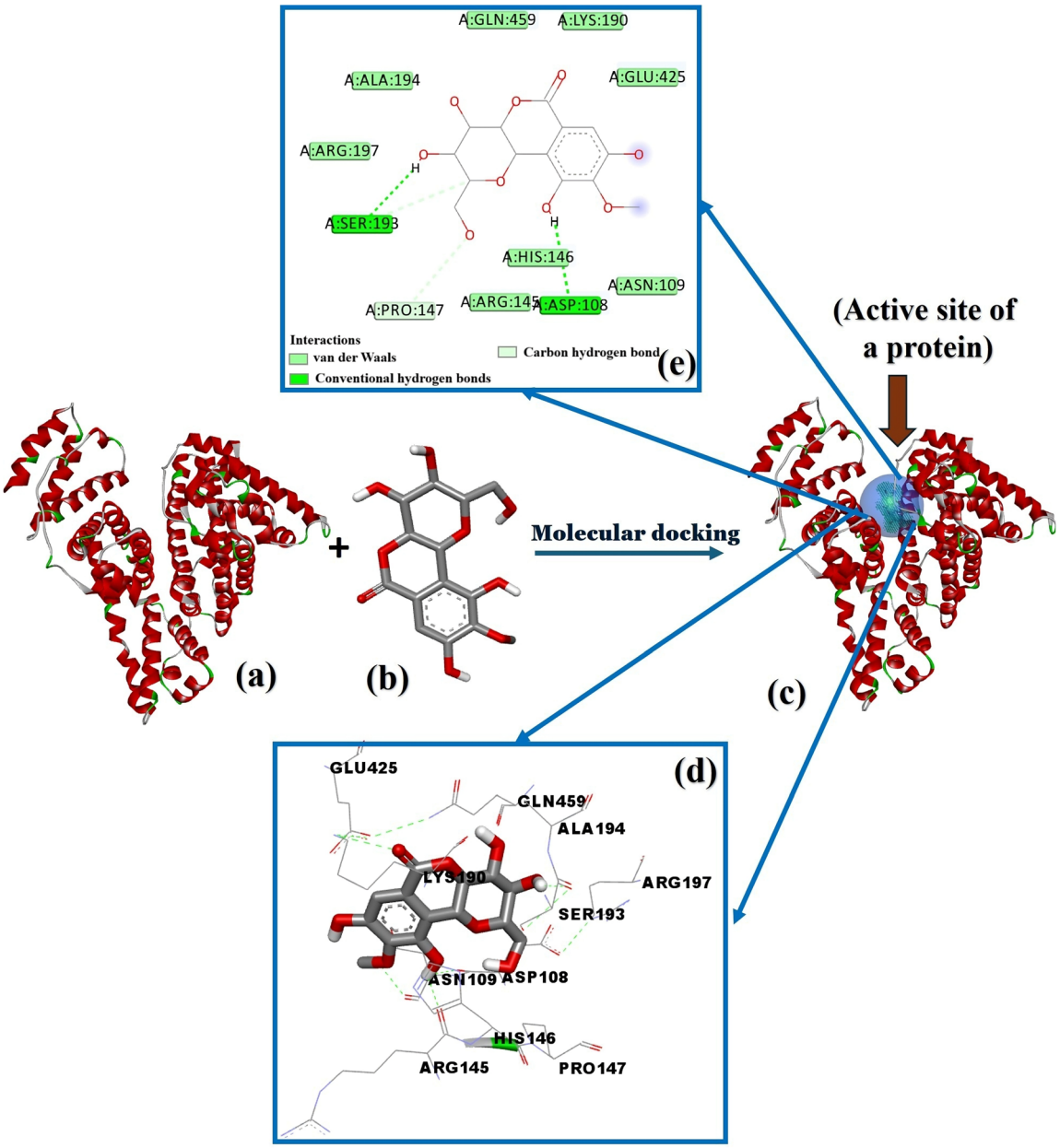

Fig. 14 Molecular docking analysis of compound *Gn*-01 with human serum albumin (HSA) (PDB ID:1AO6). (a) 3D structure of human serum albumin (HSA), (b) 3D structure of the ligand molecule used for docking (c) Docking pose of the ligand within the active site of HSA, highlighting the binding region, (d) 3D visualization of the ligand–HSA interactions, showing key interacting amino acids and hydrogen bonding, (e) 2D interaction diagram of the ligand within HSA's binding pocket, showing hydrogen bonding and other molecular interactions.

of these cavities in molecular docking and ligand binding studies.

3.10. Spectroscopic sensing of metal ions

3.10.1 By UV-vis absorption studies. The spectroscopic evaluation of compound *Gn*-01 for metal ion detection was conducted using UV-visible absorption studies in a DMSO medium. A comprehensive investigation involving various metal ions, such as Mn^{2+}, Ni^{2+}, Fe^{2+}, Cu^{2+}, and Zn^{2+}, was performed to ascertain the compound's selectivity and sensitivity. The UV-visible absorption spectrum of *Gn*-01 (10 μM) displayed two distinct bands at 246 nm and 280 nm, corresponding to n–π* and π–π* electronic transitions, respectively. These transitions indicate the electronic delocalization within the molecular structure, which plays a crucial role in interacting with metal ions.

Upon adding different metal ions in equivalent amounts, the UV-visible spectral analysis showed negligible changes in the absorption pattern, except in the presence of Cu^{2+} ions. The interaction with Cu^{2+} led to a slight redshift in the absorption peak at 246 nm, accompanied by a significant increase in peak intensity (Fig. 16). This spectral alteration suggested the

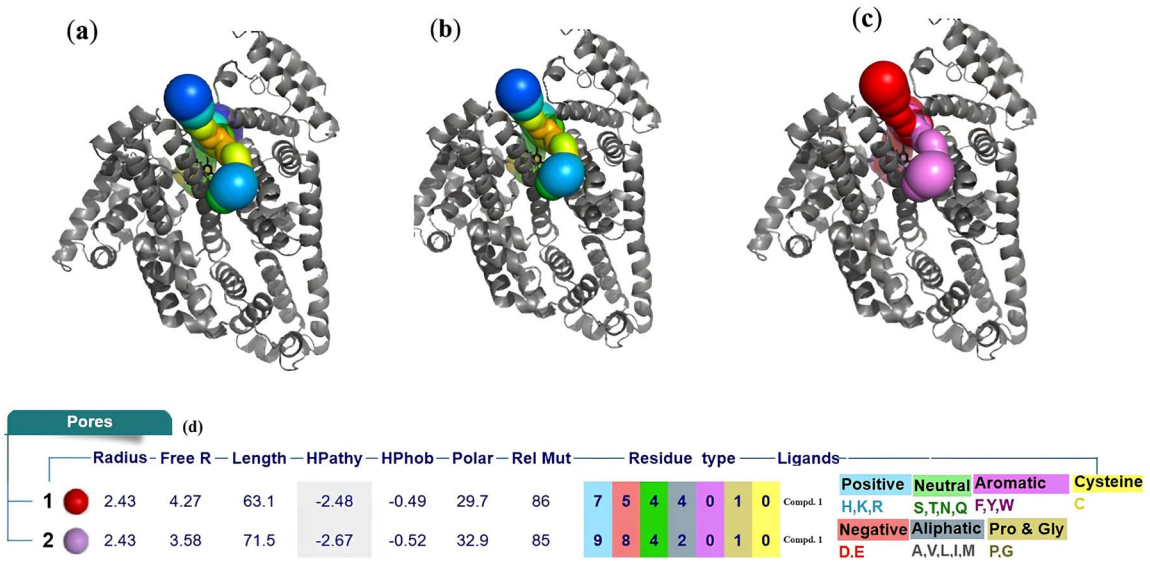

Fig. 15 Structural analysis of the two distinct pores identified within 1AO6. (a) Pores calculated on the entire protein structure, including compound *Gn*-01, colored according to their 'radius-free' value (b) Pores calculated in the absence of ligands, also colored based on their 'radius-free' value (c) Alternative pore representation highlighting differences in cavity accessibility and ligand interactions. (d) Classification of amino acid residues lining the identified pores, categorized by physicochemical properties (positive, negative, neutral, aliphatic, aromatic, proline/glycine, and cysteine), provides insights into the microenvironment and potential interaction sites within the cavities.

formation of a complex between *Gn*-01 and Cu^{2+}, which influenced the absorption characteristics.

3.10.2 Fluorescence response of compound *Gn*-01 toward metal ions. The fluorescence response of compound *Gn*-01 was systematically investigated in the presence of various metal ions, including Mn^{2+}, Ni^{2+}, Fe^{2+}, Cu^{2+} and Zn^{2+}, in a DMSO solvent system. Following excitation, the fluorescence spectra of *Gn*-01 (10 μM) exhibited a relatively low emission intensity at 372 nm. However, upon adding one equivalent of Cu^{2+} ions, a substantial enhancement in fluorescence intensity was observed, significantly surpassing the response induced by other metal ions. This distinct fluorescence amplification underscores the remarkable selectivity of *Gn*-01 for Cu^{2+} detection (Fig. 17a). Furthermore, the fluorescence response of *Gn*-01 was also measured in the presence of other biologically relevant metal ions (Ca^{2+}, Mg^{2+}, and Fe^{3+}) and compared with Cu^{2+} under the same conditions. As shown in Figure S6, these ions produced minimal or negligible changes, confirming the high selectivity of *Gn*-01 toward Cu^{2+}.

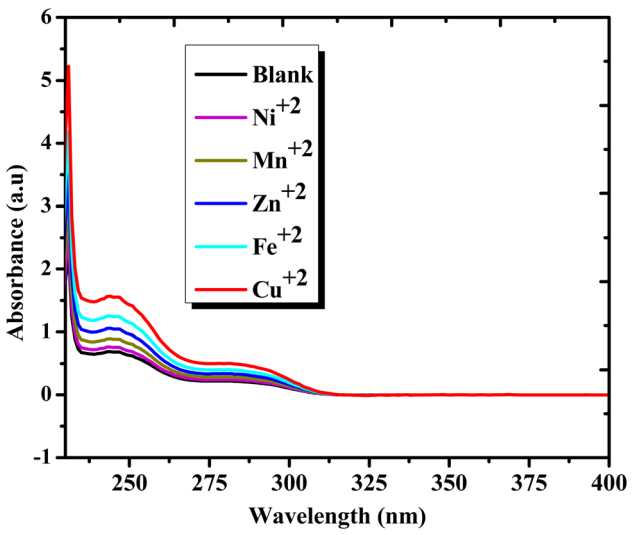

Fig. 16 UV-vis absorption spectra of *Gn*-01 in the presence of various metal ions in DMSO solution. Additionally, the broadening of the absorption spectrum for the *Gn*-01-Cu^{2+} complex could be attributed to multiple electronic transitions, including d–d transitions, π–π* transitions, metal-to-ligand charge transfer (MLCT), and ligand-to-metal charge transfer (LMCT). These distinctive spectral variations indicate that *Gn*-01 exhibits a selective response toward Cu^{2+} ions over other metal ions, making it a potential candidate for Cu^{2+} sensing applications.

The pronounced fluorescence enhancement arises from the robust coordination between Cu^{2+} and *Gn*-01, facilitating an efficient chelation-enhanced fluorescence effect (CHEF), and amplifying the emission intensity. To gain deeper insights into the selectivity and sensitivity of *Gn*-01 toward Cu^{2+}, increasing concentrations of Cu^{2+} ions (0–50 μM) were incrementally introduced, resulting in a well-defined and progressive rise in fluorescence intensity, as depicted in Fig. 17b. The emission intensity exhibited a linear correlation with the Cu^{2+} ion concentration, demonstrating the compound's exceptional capability as a highly selective and sensitive fluorescent probe for Cu^{2+} detection. This linear response confirms the strong binding affinity of *Gn*-01 toward Cu^{2+} and highlights its potential application in real-time and quantitative fluorescence-based Cu^{2+} sensing.

The interaction of *Gn*-01 with Cu^{2+} ions was systematically investigated *via* fluorescence titration, and the binding parameters were derived using the modified Stern–Volmer equation

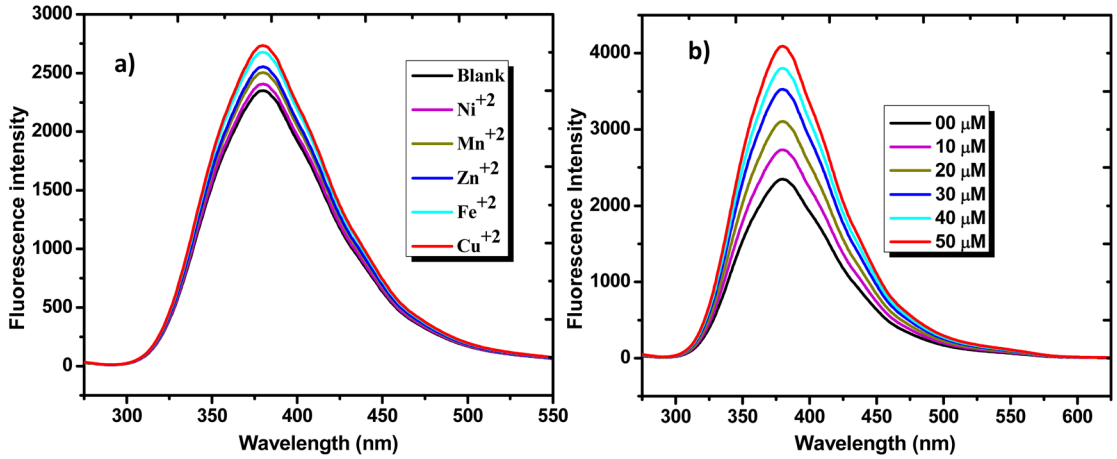

Fig. 17 (a) Fluorescence emission spectrum of compound *Gn*-01 titrating with different metal ions, and (b) emission spectrum of *Gn*-01 to increasing concentrations of Cu^{2+} (0–50 μM) in DMSO.

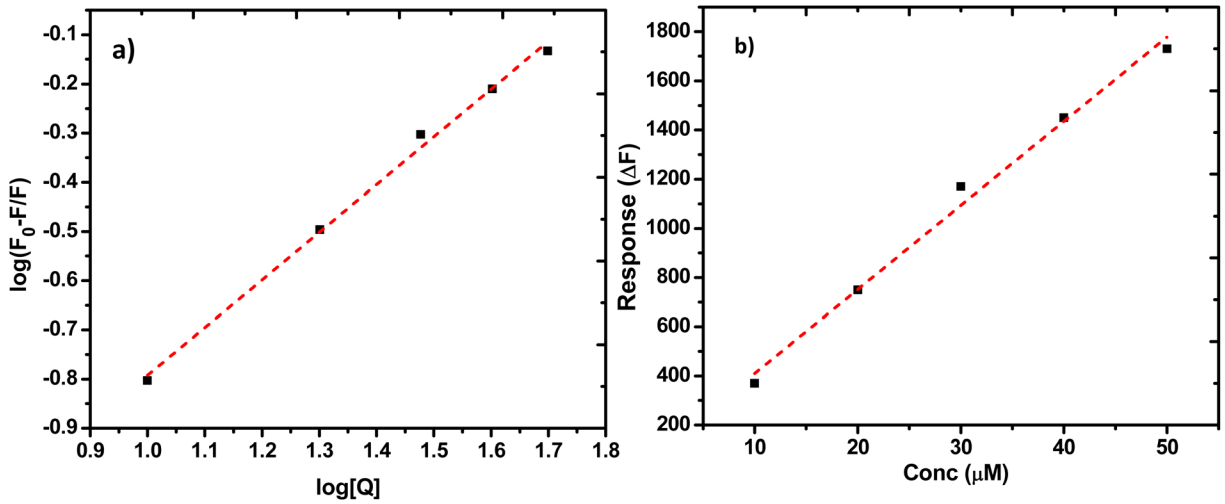

Fig. 18 (a) Modified Stern–Volmer plot, $\log[(F_0 - F)/F]$ *vs.* log[Q], used to calculate binding constant (K_b) and binding stoichiometry (n). (b) ΔF *vs.* Cu^{2+} conc. for *Gn*-01 showing the linear calibration curve for LOD determination.

(Fig. 18a). In Table 3, the binding constant ($K_b \approx 1.74 \times 10^4$ M^{-1}) reflects a moderate to strong affinity, while the binding stoichiometry ($n \approx 1$) clearly indicates the formation of a well-defined 1 : 1 *Gn*-01-Cu^{2+} complex. The limit of detection (LOD), calculated using the relation LOD = 3σ/slope (SD of the blank σ = 2.52; slope = 34.2), yielded LOD of ≈ 0.221 μM, highlighting the high sensitivity of the system. The excellent linearity (R^2 = 0.994) in Fig. 18b further confirms the reliability of the data. Mechanistically, the 1 : 1 binding stoichiometry and fluorescence response upon Cu^{2+} addition suggest that Gn coordinates with Cu^{2+} at electron-rich donor sites, most likely involving nitrogen atoms in heterocyclic moieties and/or carbonyl and hydroxyl oxygen atoms. Such coordination stabilizes the metal–ligand assembly through chelation and electrostatic interactions. Collectively, these findings highlight *Gn*-01 as an efficient and selective chemosensor for Cu^{2+} ions with promising potential in trace metal detection and environmental monitoring.

Table 3 Binding parameters of *Gn*-01-Cu^{+2} complex

Parameter	Value
Binding constant (K_b)	1.74×10^4 M^{-1}
Limit of detection (LOD)	0.221 μM
Binding stoichiometry (n)	0.969 ≈ 1
R^2	0.994

In summary, *Garcinia nervosa* is a new natural source of bergenin, providing the first crystallographic and Hirshfeld surface analysis of this molecule from this species. Importantly, the antioxidant, HSA-binding, and Cu^{2+} chemosensing properties of bergenin are reported here for the first time in the context of *G. nervosa*, with the chemosensing response arising through a fluorescence turn-on (CHEF) mechanism. Supported by molecular docking, these findings establish a comprehensive

structural-functional profile that not only differentiates this work from earlier confirmatory studies but also highlights *G. nervosa* as a promising reservoir of multifunctional bioactive molecules.

4. Conclusion

This study establishes *Garcinia nervosa* as a previously unreported source of bergenin (*Gn*-01), presenting the first single-crystal X-ray diffraction and Hirshfeld surface analysis for this species. *Gn*-01 demonstrates significant antioxidant activity ($IC_{50} = 23.438$ μg mL^{-1}) and strong, non-intercalative binding to HSA ($K_{sv} = 168.3 \times 10^4$ M^{-1}; $K_b = 3.16 \times 10^4$ M^{-1}; $n \approx 1$), with the KI quenching Stern–Volmer constant increasing from 0.59×10^4 M^{-1} (without HSA) to 4.521×10^4 M^{-1} (with HSA), as confirmed by fluorescence spectroscopy and molecular docking. Hirshfeld surface analysis highlighted the critical role of O–H···O hydrogen bonding in the crystal structure, complemented by significant H···H interactions and weaker C–H···H–C and C···O/O···C contacts, which collectively contribute to the overall packing and stability of *Gn*-01. Molecular docking on the 1AO6 protein revealed that key residues—ARG145, ASP108, and SER193—formed hydrogen bonds with *Gn*-01, stabilizing the protein–ligand complex, corroborating experimental HSA-binding results, and suggesting a favorable pharmacokinetic profile. Importantly, *Gn*-01 acts as a selective and sensitive Cu^{2+} chemosensor *via* a fluorescence turn-on (CHEF) mechanism, forming a 1 : 1 complex ($K_b = 1.74 \times 10^4$ M^{-1}; LOD $\approx$ 0.221 μM), highlighting its potential for diagnostic biosensing and therapeutic metal regulation, particularly in neurodegenerative disorders. The first report of its crystal structure, Hirshfeld analysis, HSA binding, antioxidant activity, and selective Cu^{2+} chemosensing collectively establishes *Gn*-01 as a unique bifunctional therapeutic agent with dual antioxidant, protein binding and metal-ion sensing activities. This integrated structural-functional evaluation differentiates the present work from prior studies, positioning *G. nervosa* as a valuable source of multifunctional bioactive molecules with significant antioxidant, pharmacological, and metal-ion sensing potential. Future research should focus on *in vivo* validation and mechanistic studies to fully explore its medicinal and diagnostic applications.

Conflicts of interest

The authors declare no conflicts of interest.

Data availability

Data supporting the findings of this study are available from the corresponding author upon reasonable request.

The data supporting this article have been included as part of the supplementary information (SI). Supplementary information: UV-vis, FT-IR, ^{1}H NMR, ^{13}C NMR, COSY, HMBC, and HMQC spectra of *Gn*-01 (bergenin) (Fig. S1–S5) supporting structural elucidation, SC-XRD data including Tables S1–S3, confirming the molecular structure (CCDC no. 2427544),[53] Hirshfeld surface analysis with corresponding plots, and the selectivity study of *Gn*-01 towards metal ions (Ca^{2+}, Mg^{2+}, Fe^{3+}, and Cu^{2+}). See DOI: https://doi.org/10.1039/d5ra04922a.

Acknowledgements

This work was funded by the Ongoing Research Funding Program (ORF-2025-966), King Saud University, Riyadh, Saudi Arabia.

References

1 M. Hemshekhar, K. Sunitha, M. S. Santhosh, S. Devaraja, K. Kemparaju, B. S. Vishwanath, S. R. Niranjana and K. S. Girish, *Phytochem. Rev.*, 2011, **10**, 325–351.
2 A. Paul and M. K. Zaman, *S. Afr. J. Bot.*, 2022, **148**, 39–59.
3 J. M. Kumatso and G. Sigge, *Biointerface Res. Appl. Chem.*, 2024, **14**, 102.
4 A. Kaprakkaden and A. Ali, *Phytochem. Rev.*, 2025, 1–32.
5 M. Ilyas, M. Kamil, M. Parveen and M. S. Khan, *Phytochemistry*, 1994, **36**, 807–809.
6 Universiti Teknologi Mara, *Phytochemical study and biological activities of Garcinia nervosa (CLUSIACEAE)*, Nurr Maria Ulfa Binti Seruji.
7 F. Yang, Y. Zhang and H. Liang, *Int. J. Mol. Sci.*, 2014, **15**, 3580–3595.
8 M. Fasano, S. Curry, E. Terreno, M. Galliano, G. Fanali, P. Narciso, S. Notari and P. Ascenzi, *IUBMB Life*, 2005, **57**, 787–796.
9 R. Raoufinia, A. Mota, N. Keyhanvar, F. Safari, S. Shamekhi and J. Abdolalizadeh, *J. Tabriz Univ. Med. Sci.*, 2016, **6**, 495–507.
10 J. J. Vallner, *J. Pharm. Sci.*, 1977, **66**, 447–465.
11 A. Sułkowska, *J. Mol. Struct.*, 2002, **614**, 227–232.
12 S. Naveenraj and S. Anandan, *J. Photochem. Photobiol., C*, 2013, **14**, 53–71.
13 Q. Bian, J. Liu, J. Tian and Z. Hu, *Int. J. Biol. Macromol.*, 2004, **34**, 275–279.
14 A. Sułkowska, J. Równicka, B. Bojko and W. Sułkowski, *J. Mol. Struct.*, 2003, **651–653**, 133–140.
15 P. B. Kandagal, S. Ashoka, J. Seetharamappa, S. M. T. Shaikh, Y. Jadegoud and O. B. Ijare, *J. Pharm. Biomed. Anal.*, 2006, **41**, 393–399.
16 M. Amir and S. Javed, *Int. J. Biol. Macromol.*, 2023, **241**, 124656.
17 A. Ramdass, V. Sathish, E. Babu, M. Velayudham, P. Thanasekaran and S. Rajagopal, *Coord. Chem. Rev.*, 2017, **343**, 278–307.
18 S. Montes, S. Rivera-Mancia, A. Diaz-Ruiz, L. Tristan-Lopez and C. Rios, *Oxid. Med. Cell. Longevity*, 2014, **2014**, 147251.
19 M. Scholefield, S. J. Church, J. Xu, S. Patassini, F. Roncaroli, N. M. Hooper, R. D. Unwin and G. J. S. Cooper, *Front. Aging Neurosci.*, 2021, **13**, 641222.
20 K. J. Barnham and A. I. Bush, *Curr. Opin. Chem. Biol.*, 2008, **12**, 222–228.
21 Y. Yang, J. Yan, F. Yan, Y. Yin and F. Zhuang, *J. Chem. Res.*, 2015, **39**, 590–593.

22 G. B. Bajracharya, *Fitoterapia*, 2015, **101**, 133–152.
23 D. K. Patel, K. Patel, R. Kumar, M. Gadewar and V. Tahilyani, *Asian Pac. J. Trop. Dis.*, 2012, **2**, 163–167.
24 X. Qin, Y. Yang, T. T. Fan, T. Gong, X. N. Zhang and Y. Huang, *Acta Pharmacol. Sin.*, 2010, **31**, 127–136.
25 D. K. Patel, K. Patel, R. Kumar, M. Gadewar and V. Tahilyani, *Asian Pac. J. Trop. Dis.*, 2012, **2**, 163–167.
26 P. Pandey, S. Lakhanpal, D. Mahmood, H. N. Kang, B. Kim, S. Kang, J. Choi, S. Moon, S. Pandey and S. Ballal, *Front. Pharmacol.*, 2025, **15**, 1481587.
27 P. Pandey, S. Lakhanpal, D. Mahmood, H. Na Kang, B. Kim, S. Kang, J. Choi, S. Moon, S. Pandey, S. Ballal, S. Kumar, F. Khan, B. Kim, S. Kumar Mishra, T. M. Karpiński and R. Prakash Shukla, *Front. Pharmacol*, 2025, **15**, 1481587.
28 R. A. Costa, J. N. da Silva, V. G. Oliveira, L. M. Anselmo, M. M. Araújo, K. M. T. Oliveira and R. D. C. S. Nunomura, *J. Mol. Liq.*, 2021, **330**, 115625.
29 R. Subramanian, P. Subbramaniyan and V. Raj, *Beni-Suef Univ. J. Basic Appl. Sci.*, 2015, **4**, 256–261.
30 Z. M. Salimo, M. N. Yakubu, E. L. da Silva, A. C. G. de Almeida, E. V. Costa, F. M. A. da Silva, J. F. Tavares, W. M. Monteiro and G. C. de Melo, *Biomolecules*, 2023, **13**, 403.
31 M. Ilyas, M. Perveen, N. Shafiullah and S. M. Ahmad, *J. Chem. Res.*, 2002, **2002**, 231–233.
32 N. Abu, W. Y. Ho, S. K. Yeap, M. N. Akhtar, M. P. Abdullah, A. R. Omar and N. B. Alitheen, *Cancer Cell Int.*, 2013, **13**, 102.
33 K. Juvale, V. F. S. Pape and M. Wiese, *Bioorg. Med. Chem.*, 2012, **20**, 346–355.
34 J. van Jaarsveldt, C. Marais, J. H. van Tonder and B. C. B. Bezuidenhoudt, *Synthesis*, 2023, **55**, 2742–2756.
35 N. Shahabuddin, N. Uzma, M. Azam, M. Parveen, N. H. A. Kadir, K. Min and M. Alam, *RSC Med. Chem.*, 2024, **15**, 3889–3911.
36 A. Aslam, N. Uzma, U. H. Al Hoqani, M. Parveen, S. N. H. Azmi and M. Alam, *ACS Omega*, 2025, **10**, 19750–19763.
37 A. Kumar, N. Uzma, S. Al Kindi, M. Amir, S. N. H. Azmi, S. Javed, M. Parveen and M. Alam, *Arabian J. Chem.*, 2025, **18**, 2672024.
38 R. A. Costa, J. N. da Silva, V. G. Oliveira, L. M. Anselmo, M. M. Araújo, K. M. T. Oliveira and R. D. C. S. Nunomura, *J. Mol. Liq.*, 2021, **330**, 115625.
39 M. Parveen, N. Uzma, A. A. Khan, S. A. A. Nami, R. Kataria, A. Malik, N. A. M. Amali, N. H. Abd Kadir and M. Alam, *ACS Omega*, 2024, **9**, 39484–39502.
40 M. Siddiqui, S. Verma, M. Naushad and M. Ali, *J. Mol. Liq.*, 2025, **437**, 128494.
41 M. Parveen, N. Uzma, A. A. Khan, W. N. D. Wan Fauzi, N. H. Abd Kadir, M. Siddiqui and M. Alam, *ACS Omega*, 2025, **10**, 34895–34916.
42 M. Parveen, N. Uzma, M. Azam, M. Azeem, A. Aslam, M. Bashir and M. Alam, *J. Saudi Chem. Soc.*, 2024, **28**, 101881.
43 M. Parveen, S. Azaz, A. Zafar, F. Ahmad, M. R. Silva and P. S. P. Silva, *J. Photochem. Photobiol., B*, 2017, **167**, 176–188.
44 P. R. Spackman, M. J. Turner, J. J. McKinnon, S. K. Wolff, D. J. Grimwood, D. Jayatilaka and M. A. Spackman, *J. Appl. Crystallogr.*, 2021, **54**, 1006–1011.
45 N. M. Karaush-Karmazin, B. F. Minaev, V. A. Minaeva, O. O. Panchenko and H. Ågren, *Eurasian J. Chem.*, 2024, **29**, 43–55.
46 H. M. Berman, *Nucleic Acids Res.*, 2000, **28**, 235–242.
47 O. Trott and A. J. Olson, *J. Comput. Chem.*, 2010, **31**, 455–461.
48 G. M. Morris, R. Huey, W. Lindstrom, M. F. Sanner, R. K. Belew, D. S. Goodsell and A. J. Olson, *J. Comput. Chem.*, 2009, **30**, 2785–2791.
49 F. Shakeel, R. A. Mothana, N. Haq, N. A. Siddiqui, M. M. Al-Oqail and A. J. Al-Rehaily, *J. Mol. Liq.*, 2016, **220**, 823–828.
50 T. Zhao, J. Zhang, B. Guo, F. Zhang, F. Sha, X. Xie and X. Wei, *J. Mol. Liq.*, 2015, **207**, 315–322.
51 T. Zhao, F. Sha, J. Xiao, Q. Xu, X. Xie, J. Zhang and X. Wei, *Fluid Phase Equilib.*, 2015, **405**, 7–16.
52 Y. Yue, J. Liu, R. Liu, Q. Dong and J. Fan, *Spectrochim. Acta, Part A*, 2014, **124**, 46–51.
53 CCDC 2427544: Experimental Crystal Structure Determination, 2025, DOI: **10.5517/ccdc.csd.cc2mh1w2**.